

Predicting large scale cosmological structure evolution with GAN-based autoencoders

Marion Ullmo^{1,2,3}, Nabila Aghanim², Aurélien Decelle^{3,4}, and Miguel Aragon-Calvo⁵

¹ IRFU, CEA, Université Paris-Saclay, Gif-sur-Yvette, France

² Université Paris-Saclay, CNRS, Institut d'Astrophysique Spatiale, Bâtiment 121 Campus Paris-Sud 91405, Orsay, France

³ Université Paris-Saclay, CNRS, TAU team INRIA Saclay, Laboratoire de recherche en informatique, 91190, Gif-sur-Yvette, France.

⁴ Departamento de Física Teórica, Universidad Complutense, 28040 Madrid, Spain

⁵ Instituto de Astronomía, UNAM, Apdo. Postal 106, Ensenada 22800, B.C., México

ABSTRACT

Cosmological simulations play a key role in the prediction and understanding of large scale structure formation from initial conditions. We make use of GAN-based Autoencoders (AEs) in an attempt to predict structure evolution within simulations. The AEs are trained on images and cubes issued from respectively 2D and 3D N-body simulations describing the evolution of the dark matter (DM) field. We find that while the AEs can predict structure evolution for 2D simulations of DM fields well, using only the density fields as input, they perform significantly more poorly in similar conditions for 3D simulations. However, additionally providing velocity fields as inputs greatly improves results, with similar predictions regardless of time-difference between input and target.

Key words. (Astronomical instrumentation, methods and techniques:) Methods: statistical, Methods: data analysis

1. Introduction

Cosmological simulations allow us to confront existing theoretical models – describing the universe's initial state, contents, and the physical processes governing its evolution – to increasingly detailed observations of the cosmos, such as that of the James Webb Space Telescope (Gardner et al. 2006), or of the upcoming Euclid survey (Laureijs et al. 2011).

These simulations can describe the evolution through time of matter on a large scale, from N-body simulations modeling only the gravitational interaction of massive particles in expanding space (such as the Millenium simulation (Boylan-Kolchin et al. 2009)), to more complex simulations (e.g. Illustris (Vogelsberger et al. 2014), IllustrisTNG (Nelson et al. 2019), EAGLE (Crain et al. 2015)) incorporating hydrodynamics and/or physical processes on relatively small scales modeling the evolution of the baryonic matter.

When considering the N-body problem, one must keep in mind that there is no known closed-form expression that can be used to directly calculate the positions and velocities of the particles at any given time. Indeed, the gravitational force between each pair of DM particles in simulations depends on their positions and masses, and the resulting motion is influenced by the collective interactions among all the particles, entailing a highly nonlinear evolution of the system in time. Current numerical methods approach this problem by starting with initial conditions of particle positions and velocities, and iteratively resolving the equations of motion on time steps small enough that a linear evolution can sufficiently approximate particles' true motion.

However, as computations scale with the square number of particles, this can quickly prove very costly in terms of time and computing power. This in turn limits the scale or resolution with which to conduct a simulation.

While faster fully analytical approaches (Shandarin & Zel'dovich 1989; Kitauro & Heß 2013) and semi-analytical simulations that combine traditional simulation methods and analytical approximations (Monaco et al. 2002; Tassev et al. 2013) both relying on first- or second-order perturbation theory exist, they cannot address the highly nonlinear stages of the structure formation.

Lately, machine learning (ML) approaches have proved efficient in completing tasks for which prescriptive analytical approaches were either slow, too approximative or non-existent. Examples in astronomy include classification (e.g. galaxy types (Shamir 2009; Freed & Lee 2013; Biswas & Adlak 2018) or cosmic web structure types (Aragon-Calvo 2019)), redshift estimation (Henghes et al. 2021; Rastegarnia et al. 2022; D'Isanto & Polsterer 2018; Henghes et al. 2022), detection of various objects of interest (Rezaei et al. 2022b; Vafaei Sadr et al. 2019; Jia et al. 2023; González et al. 2018), anomalies (Reyes & Estévez 2020; Dere et al. 2021; Villar et al. 2021), or physical effects like gravitational lensing (Rezaei et al. 2022a; Wilde et al. 2022) or Sunyaev-Zel'dovich (SZ) effects (Tanimura et al. 2022; Bonjean 2020), deblending sources (Burke et al. 2019; Hausen & Robertson 2022; Hansen et al. 2022), determining baryonic matter properties given dark matter distribution (Jo & Kim 2019; Wu & Jespersen 2023; Chittenden & Tojeiro 2023; Bonjean et al. 2019), simulation augmentation (Sweere

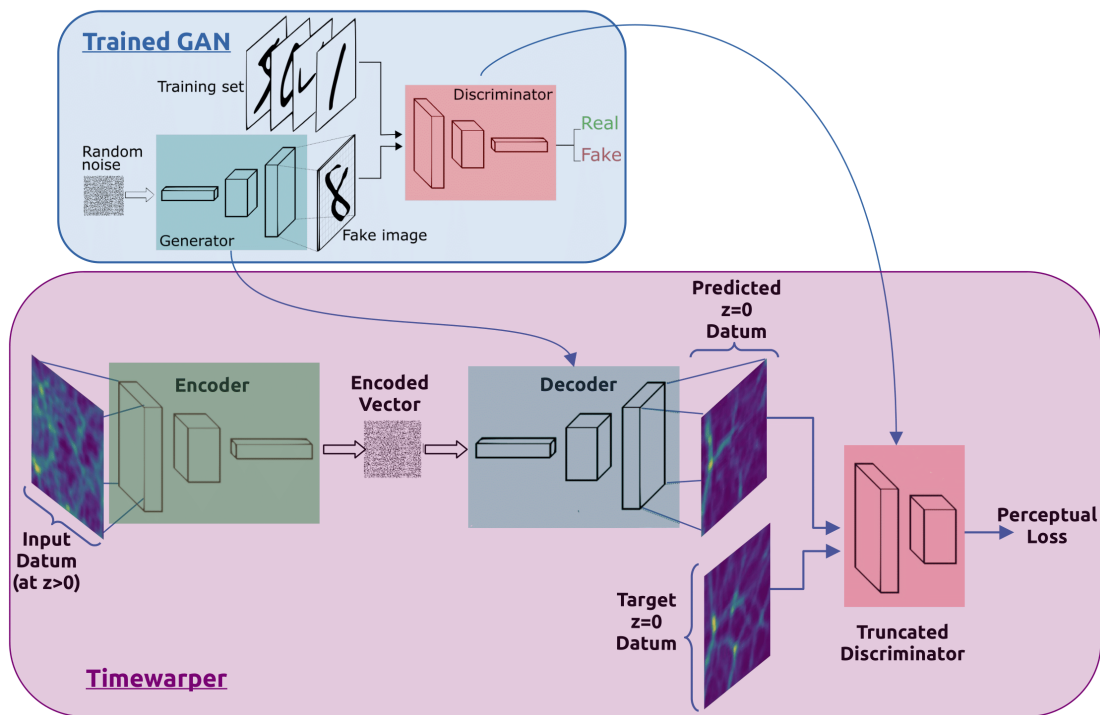


Fig. 1: Architecture of the timewarper. A trained GAN’s generator is used as a readily built decoder. Only the encoder’s weights are changed during training. The same GAN’s truncated discriminator is used to compute a perceptual loss¹.

et al. 2022; Kodi Ramanah et al. 2020; Agarwal et al. 2018), etc. . .

More specifically when considering the time evolution of complex physical systems, several NN-based experiments (Feng 2023; Wiewel et al. 2019; Liu 2023; Humbird et al. 2018) have shown promising results in terms of emulating simulations, and more specifically cosmological simulations (He et al. 2019; Sanchez-Gonzalez et al. 2020; Conceição et al. 2024).

In this article, we inquire about the ability for neural networks to infer the evolution over time of large-scale density fields, and the methods to optimize this inference. This prospective work, by providing a proof of concept, aims to establish the relevance of using neural networks as a fast alternative to analytical approximations for N-body simulations, while offering insight on methods to optimize prediction accuracy.

In previous work (Ullmo et al. 2021), we presented a GAN-based autoencoder (AE) that was able to encode high-dimensional simulation data (2D 128²-pixel and 3D 64³-voxel density maps) into low-dimensional data (100- and 200-vectors).

Here we further experiment with and build upon this AE, now training it to predict the evolution of simulation-based density maps from early time (redshifts $z = 1, 2$ and 3) to the current time ($z = 0$). We refer to this predictive AE as *timewarper* (TW).

In Sec. 2, we outline the setup of our experiment, wherein we describe the architecture and training of our TWs, the data used for training, and the metrics by which we measure the quality of our results. In Sec. 3.1 we begin by showing results for a TW trained to predict simply from an input

density map; we refer to it as "baseline TW". In Sec. 3.2, we introduce a TW trained with additional input information in the form of the density field’s associated velocity field, which shows significant improvement on the baseline approach. We refer to it as "velocities TW". In Sec. 4 we interpret results and discuss other possible optimization methods. Finally we conclude in Sec. 5.

2. Setup

Our goal is to create a network capable of forecasting the evolution of a simulation-derived data set (a discrete 2D or 3D density map generated from a 2D or 3D N-body simulation) from previous instances (when $z > 0$) to the current time ($z = 0$).

Thus, we build a TW that takes a datum in the form of a simulated density field at a given fixed redshift (namely $z = 0, 1, 2$ or 3) as input and is tasked with recovering its corresponding simulation at $z = 0$, by minimizing the distance (see eq.1) between its output and target datum. In a second step, we provide the TW an associated velocity field, in an effort improve the AE’s predictions.

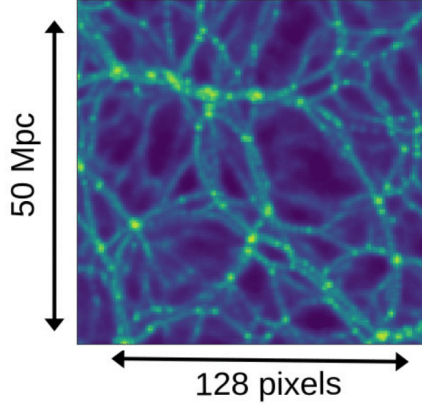
Below, we briefly present the networks, data and metrics used for our work.

2.1. Networks

2.1.1. GANs in a nutshell

GANs, or generative adversarial networks, are notorious for their ability to emulate data from a training set, typically in the form of images. They consist of a pair of deep neural networks that are trained simultaneously in an adversarial

2D simulation data (images)



3D simulation data (cubes)

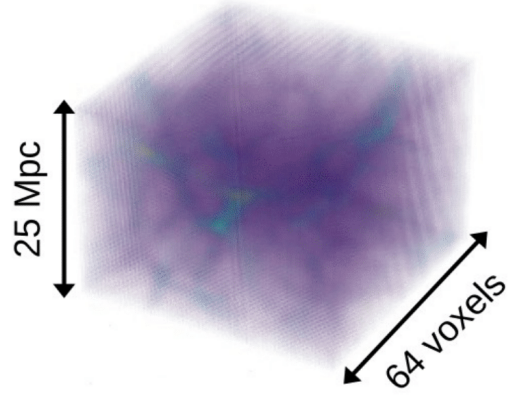


Fig. 2: Example of simulation-issued data: a 2D image from a 2D simulation (*left*) and a 3D cube (*right*) from a 3D simulation. They are built by dividing an N-body simulation snapshot into pixels (or voxels) and counting the particles within each, creating a discrete density map. The map is then smoothed with a Gaussian filter and log-transformed, allowing cosmic structure to stand out starkly. Doing so creates data that is compatible with convolutional neural networks, which specialize in feature detection.

manner (see top diagram in Fig.1). The first, a generator, intakes a vector with randomly distributed values and is trained to output realistic data by "fooling" the second, a discriminator, which is tasked with separating genuine training data from data generated by the generator. Throughout training they become gradually better at their respective tasks, simultaneously increasing the difficulty of the other's task. Once trained the generator is able to output a training set-like datum from a low-dimension input vector, while the discriminator is capable of distinguishing high-level features in data to suit its task. We make use of these properties to build our AEs.

2.1.2. Timewarpers

Our work rests on the use of AEs based on these convolutional GANs (the TW, displayed in Fig.1, bottom).

The AEs consist of an encoder which intakes a datum at a given redshift $z \geq 0$ and encodes it into a vector within a low-parameter latent space with greater semantic significance. This encoded vector is then fed into a decoder tasked with recovering the original datum at redshift $z = 0$, through minimization of the loss described below (eq.1).

To constrain the decoder to output data that would be statistically consistent with true $z = 0$ data, we rely on a GAN that has been previously trained to generate simulation-like data at $z = 0$, first by using this GAN's generator (made to output simulation-like data at $z = 0$) as the decoder and locking its weights during training, second by using the GAN's truncated discriminator as part of the AE's loss¹.

$$L_{AE} = \Delta(x, \tilde{x}) \quad (1)$$

where x is the output datum (i.e the AE's prediction of input datum at $z = 0$), \tilde{x} is the ground truth (true input

¹ See initial article (Ullmo et al. 2021)

datum at $z = 0$) and Δ is the ℓ_2 difference in the truncated discriminator's latent space.

This type of loss, termed perceptual loss (Johnson et al. 2016), integrates a discriminator's capability to emphasize the features and patterns of data rather than relying solely on a basic pixel-by-pixel comparison.

Input shape	128×128
Filter sizes	{5, 5, 5, 5}
$n_{filter}(E)$	{32, 64, 128, 256, 512}
$n_{filter}(D)$	{256, 128, 64, 32, 1}
Strides:	{2, 2, 2, 2}
Layer Activation	Leaky ReLU (E), ReLU (D)
Final Activation	None(E), Tanh (D)
Latent dimension	100

(a) Architecture specifications for each layer of the 2D TW's encoder (E) and decoder (D).

Input shape	$64 \times 64 \times 64$
Filter sizes	{4, 4, 4, 4}
$n_{filter}(E)$	{32, 64, 128, 256}
$n_{filter}(D)$	{128, 64, 32, 1}
Strides:	{2, 2, 2, 2}
Layer Activation	Leaky ReLU (E), ReLU (D)
Final Activation	None(E), Tanh (D)
Latent dimension	200

(b) Architecture specifications for each layer of the 3D TW's encoder (E) and decoder(D).

Fig. 3: Architectures of the 2D and 3D TW. They are both trained using the *Adam* optimizer with the same parameters as above ($lr = 0.0002, \beta_1 = 0.5$).

2.2. Data

2.2.1. Simulations

Our networks are trained on data built from both 2D and 3D N-body simulations.

The 2D data (Fig. 2, left) provide us with simpler conditions (lower-parameter problem, in terms of particle degree of freedom, datum size and network size), leading to more optimal results for a more ideal proof of concept and a point of comparison for 3D results. The training set is built from 1000 snapshots from nbody2D² simulations, a set of 2D particle-mesh N-body simulations of side $100Mpc/h$ with 512^2 particles using the standard Λ CDM cosmology. They are run and saved for redshifts $z = 0, 1, 2$ and 3 .

The training set for the 3D data (Fig. 2, right), our data of interest, is built from a single snapshot of a GADGET2 simulation (Springel et al. 2001; Springel 2005) of side $100Mpc/h$ with 512^3 particles using standard Λ CDM cosmology and saved at redshifts $z = 0, 1, 2$ and 3 .

2.2.2. Training Data

Individual data are built in the following way: each (2D or 3D) snapshot is made into a discrete (256×256 or $256 \times 256 \times 256$, respectively) density map which is subsequently smoothed and log-transformed for compatibility with the neural network. From these, smaller sub-arrays (of side $50Mpc/h$ and 128 pixels for 2D and $25Mpc/h$ and 64 voxels for 3D) are extracted to make up the training sets. This gives us respectively $5 \cdot 10^8$ and $8 \cdot 10^8$ possible sub-arrays. Given this high number of possibilities and the redundancy within them, we do not reason in terms of epochs for training time where one epoch corresponds to the network processing the entire training set. Instead we quantify training time in terms of gradient updates performed on data batches (of size 200 in our case), with each training batch randomly selected from all possible sub-arrays.

In a second part of our work, we additionally provide the density fields' associated velocity fields as input for the 3D case. We follow a similar approach as the density field to build the velocity field. Dividing the snapshot space into $3 \times 256 \times 256 \times 256$ voxels, we compute three 3D averaged velocity fields for each direction (x, y, z), by summing the velocities of the particles in each voxel and dividing the sum by the number of particles. Inspecting the resulting cubes, we find that cosmic structures are visually apparent without need for log-transformation. Thus we simply apply a normalization of voxel values:

$$v' = v/N \quad (2)$$

Where v' is the new velocity and N is fixed such that $|v'|_{max} \lesssim 1$. This done, we apply the same smoothing as for the 3D density to obtain our final three $256 \times 256 \times 256$ velocity fields for each (x, y and z) direction.

Combining the density field with the velocity fields thus constructed, we are equipped with an array of size $256 \times$

² credit: Johannes Hidding https://zenodo.org/record/4158731#.X5_ITJwo-Ch

$256 \times 256 \times 4$ from which we extract smaller arrays of size $64 \times 64 \times 64 \times 4$.

2.3. Metrics

To quantify the efficiency of the TW's prediction, we rely on two metrics; the power spectrum to ensure that the predicted data is statistically consistent with target data, and the dice coefficient (see Ullmo et al. (2021) for further details) to ensure that the dense structures in an individual datum are precisely recovered.

The power spectrum for a frequency ν it is given by:

$$P(\nu) = \langle \|A_{kl}\|^2 \rangle_{(k,l)|k^2+l^2=\nu^2}, \quad (3)$$

where $A_{k,l}$ are the image's discrete Fourier transform elements, and the dice coefficient for a pair of images/cubes a and b , is expressed in the following way:

$$O_{ab}(t) = \frac{N_{ab}(t)}{N_a(t) + N_b(t)} \quad (4)$$

Where $N_{a/b}(t)$ is the number of pixels/voxels whose value is above the threshold t in a or b and $N_{ab}(t)$ is the number of pixels/voxels whose value is above t for both a and b in a given position in an image/cube.

3. Results

3.1. Baseline TW results

We input a datum in the form of a density field at a given redshift $z > 0$ and constrain the TW to output the equivalent $z = 0$ density field (with two "equivalent" density fields referring to the same comoving region within a snapshot at the two redshifts considered for input and target $z_{ini} \rightarrow z_{fin}$) by minimizing the perceptual loss (see Eq.1).

We do this for both 2D and 3D data.

3.1.1. 2D images

We first focus on the outcome of the TW trained to recover density fields at redshift $z = 0$ for the set of 2D simulation images, from input density fields at redshifts varying from $z = 0$ to $z = 3$ by steps of $\Delta z = 0.5$.

One might note that "predictions" from $z = 0$ to $z = 0$ consist in simple replicative autoencoding and define the limitations of our setup, the discrepancy between input and output in this case being strictly due to encoding loss rather than inaccurate prediction.

We compare our results on predictions from higher redshifts to this $z = 0$ reference. The task is expected to be harder the higher the input z ; indeed, given that the development of structure in matter is a highly non-linear process, we can expect that the farther away in time the target is from the output, the farther the density field will steer from an easily approximated linear evolution.

For all $z > 0 \rightarrow z = 0$ input-output pair, a distinct TW is individually run for 15k gradient updates (no significant

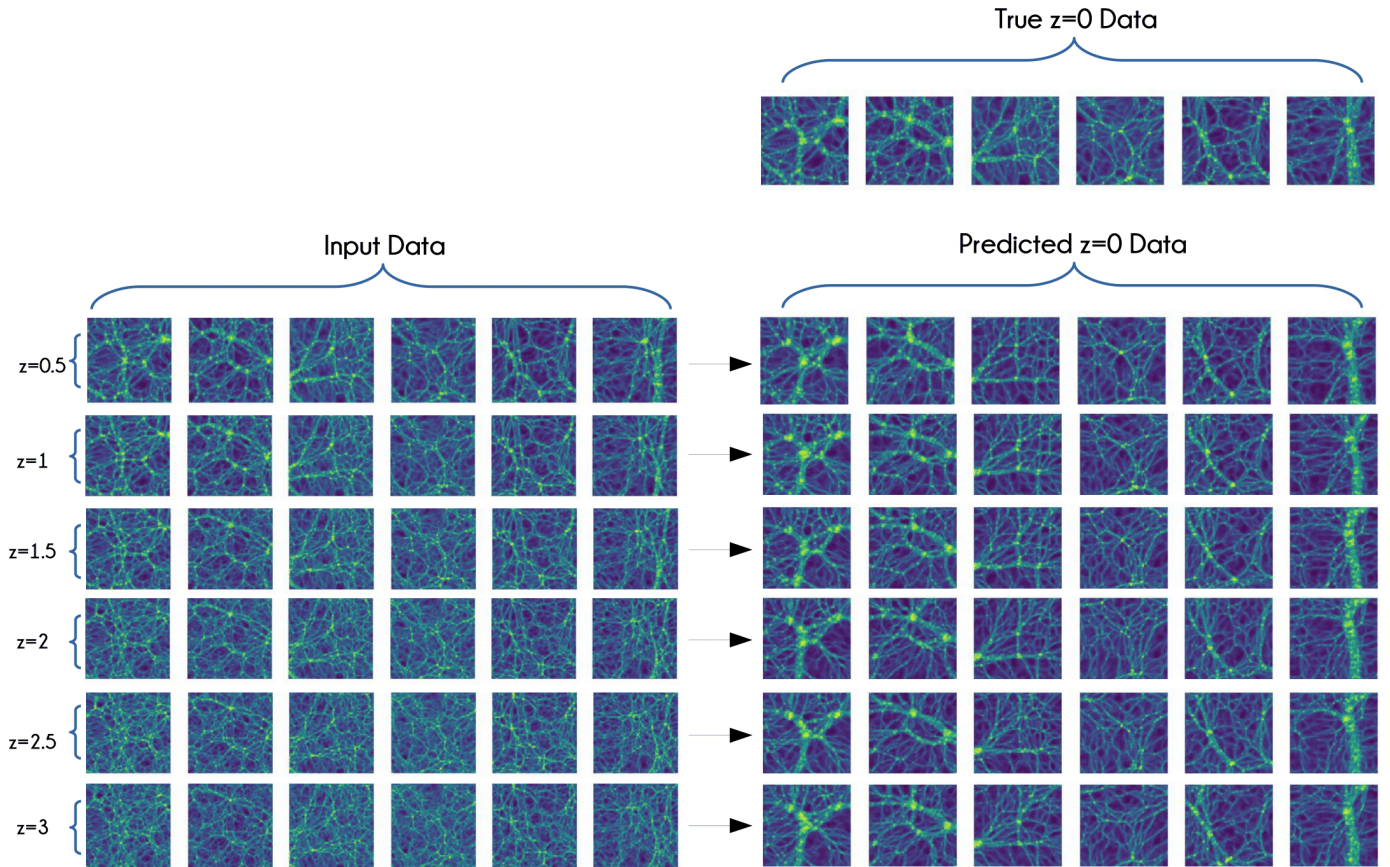


Fig. 4: Six images from the 2D simulations at various redshifts (*left*), and their equivalent predictions of redshift $z = 0$ (*right*) as inferred by the *baseline TW*. The true $z = 0$ simulation images are shown above the predicted images (*upper right*) for comparison.

improvement observed for longer training), and the best weights are recovered by finding the minima of validation losses computed every 1000 update for each input z (0.5, 1, 1.5, 2, 2.5, 3), respectively at 10, 15, 15, 10, 15, and 12k updates.

We illustrate the baseline TW’s performance in recovering $z = 0$ from different redshifts with a set of six simulation images taken at random from the test set (Fig. 4). These data are taken at various redshifts (left block) and used as input for the trained TWs to predict their $z = 0$ equivalent (upper right). Predicted data are shown in the right block.

We find that regardless of input redshift, the TWs are successful in recovering $z = 0$. The larger and denser structures are consistently well recovered while finer details exhibit more variability. Initially, it is difficult to discern any perceptible changes in performance based on varying input redshifts; indeed, structures appear to be reliably predicted even when inferring from higher redshifts. However, upon closer examination, we note that as the input redshift increases, there is a gradual loss of detail in the predicted structures. This loss manifests as the merging of certain large structures, shifts or disappearance of finer structures, and alterations in the positions of overdense regions.

Inspecting the power spectrum of the predicted data (Fig. 5, *left*), we find that the TWs seem to recover similar statistics regardless of the input z ; all predicted spectra have the

expected shape, but a similar upward shift at lower frequencies compared to the true data. This suggests that denser regions are recovered with slightly excessive density.

Finally, we observe the Dice coefficient (fig. 5, *right*); while predictions from all redshifts show similar results to the baseline AE’s, we can see quite clearly that for every increment of input z , the obtained dice coefficient is slightly lower than the previous at all pixel thresholds, exhibiting the increased difficulty of the predictive task with an increased input z .

From this first test of the TW on 2D data, we can conclude that, in this simple case at least, our networks can predict structure evolution quite satisfactorily in the time spans considered. Unsurprisingly, predictions are more precise the closer in time the input is to the target, and we obtain best results for $z = 0$ to $z = 0$ encoding.

3.1.2. 3D cubes

We now focus on the outcome of the TW trained to recover density fields at redshift $z = 0$ for the set of 3D simulation cubes, from input density fields at redshifts varying from $z = 0$ to $z = 3$ by steps of $\delta z = 1$. The baseline TW is run for 30k gradient updates, and the best weights are recovered for each input $z = (0, 1, 2, 3)$, respectively at 30, 30, 20, and 30k updates. Indeed, beyond a certain threshold the

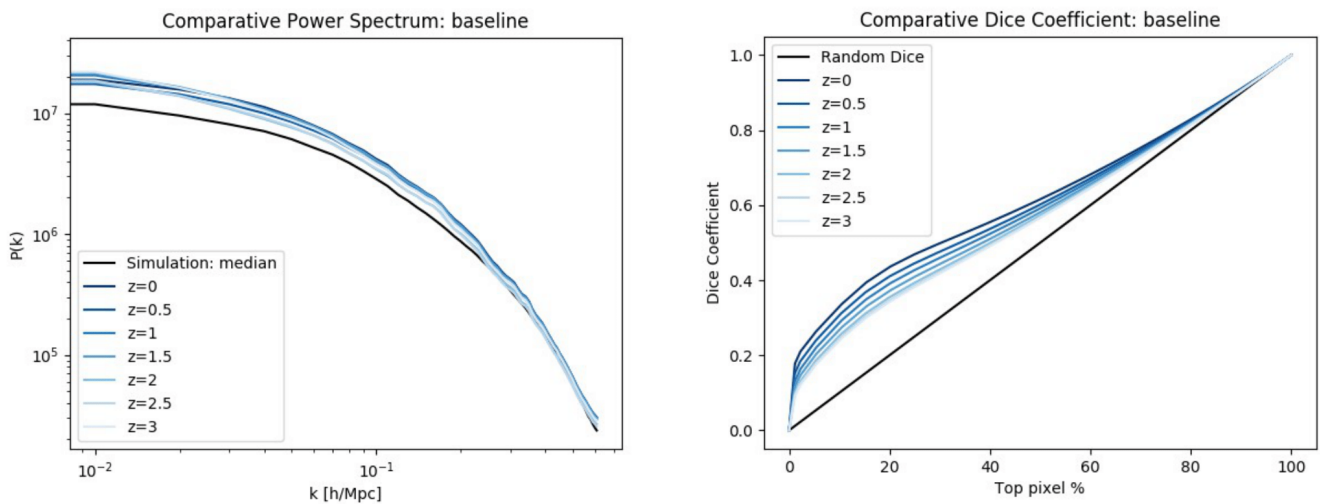


Fig. 5: *Left*: Median power spectra of the 2D data predicted by the *baseline TW* from various redshifts (*blue*). The median power spectrum of the true $z = 0$ simulation data is shown in *black*. *Right*: Average dice coefficient between target $z = 0$ 2D simulation data and data as predicted by the *baseline TW* from various redshifts.

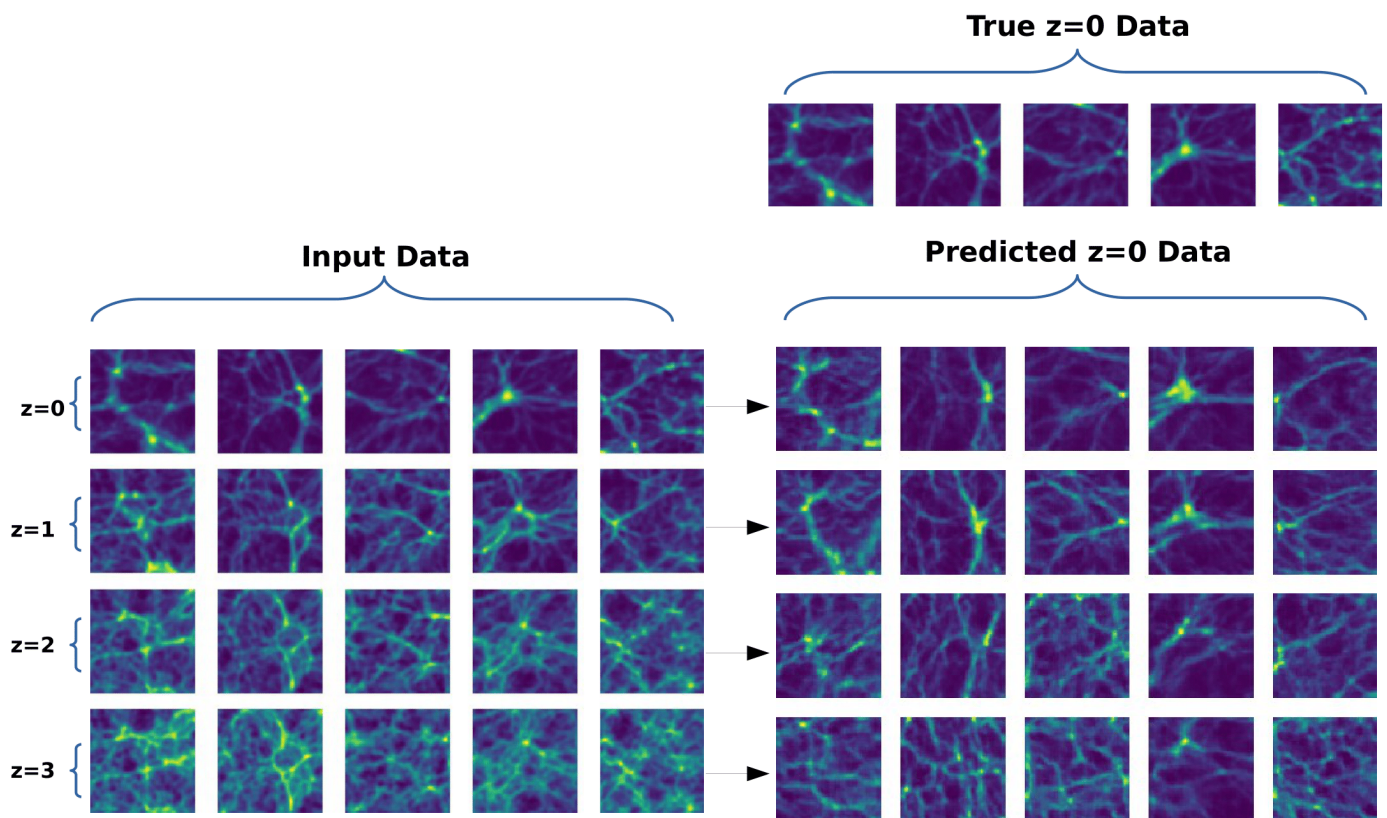


Fig. 6: Five images from the 3D simulations at various redshifts (*left*), and their equivalent predictions of redshift $z = 0$ (*right*) as inferred by the *baseline TW*. The true $z = 0$ simulation images are shown above the predicted images (*upper right*) for comparison.

progression of loss appears to exhibit a linear pattern when plotted on a log-log scale. We halt training at 30k updates due to time constraints.

We observe five simulation cubes taken at random from the test set (Fig. 6). These data are taken at various redshifts (*left block*) and used as input for the trained TWs to predict

their $z = 0$ equivalent (*upper right*). Predicted data are shown in the right block.

Here, we find that, contrary to the 2D case, the predicted data become noticeably more imprecise - that is to say, we start to see disappearing high density contrast while spurious low-density structures arise - with the increase of the input

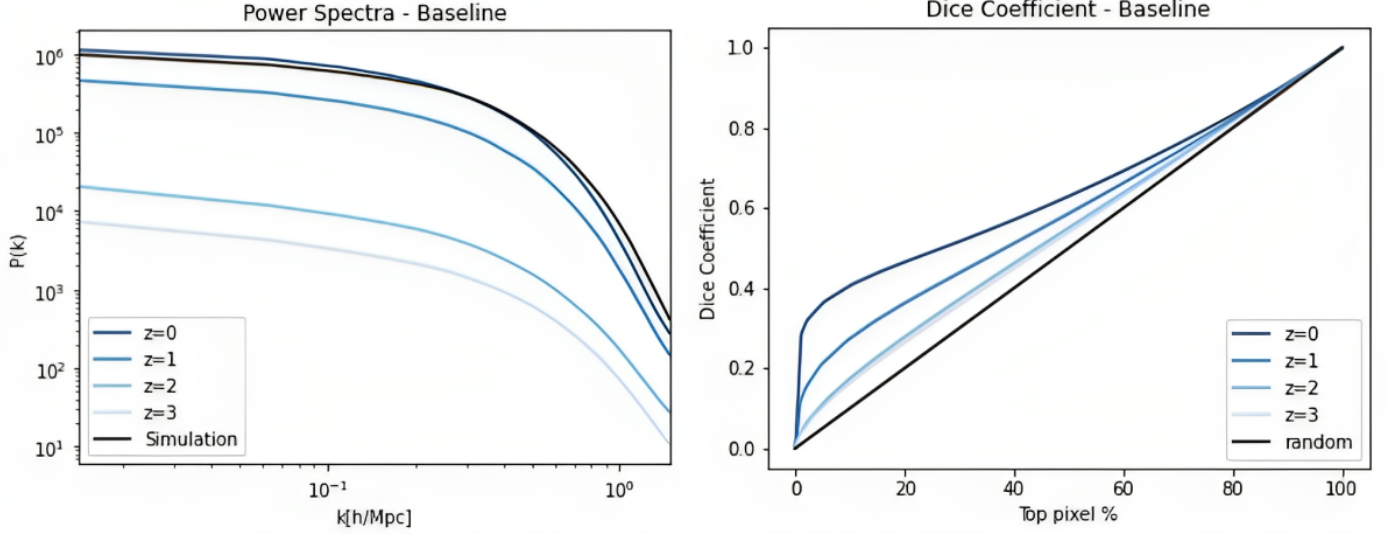


Fig. 7: *Left*: Median power spectra of the 3D data predicted by the *baseline TW* from various redshifts (*blue*). The median power spectrum of the true $z = 0$ simulation data is shown in *black*. *Right*: Average dice coefficient between target $z = 0$ 3D simulation data and data as predicted by the *baseline TW* from various redshifts.

redshift, with data predicted from $z = 2$ and $z = 3$ showing very little similarity to the target $z = 0$ data.

We can note that when provided with this progressively less informative (i.e. the density field at progressively earlier states), the network increasingly tends to default to outputting data that shows few to no dense structures and is less correlated with the correct output, opting for more diffuse structure that can blend in with any target data's background, thus reducing on average the difference between prediction and any random target.

Given the previous observations, it is not surprising to find that the power spectrum (see Fig.7, *left*) of the predicted data becomes lower for high z inputs, since the lack of dense structures leads to overall lower density and a loss of signal at all frequencies. However in terms of shape, the power spectrum seems to be well recovered.

Finally, we examine the Dice coefficient (Fig.7, *right*); once more the increased disparity between prediction and target with higher input z is made clear, with overall dice becoming significantly lower for input $z = 1$ compared to $z = 0$ and for inputs $z = 2$ and 3 compared to $z = 1$.

Overall we can observe that the networks perform much more poorly on our 3D data compared to 2D.

3.2. Introducing the velocity field

Additional information in the form of input density fields' associated velocity fields (see Fig.8) is bound to constrain more thoroughly the target density fields, as initial velocities notably provide the necessary information for a linear evolution of the density field.

These velocity fields can be obtained from the snapshots. Indeed, in their raw form and for every saved snapshot, our N-body simulations provide us with every particle's position, but also every particle's velocity, in the form of a 3D vector for each particle.

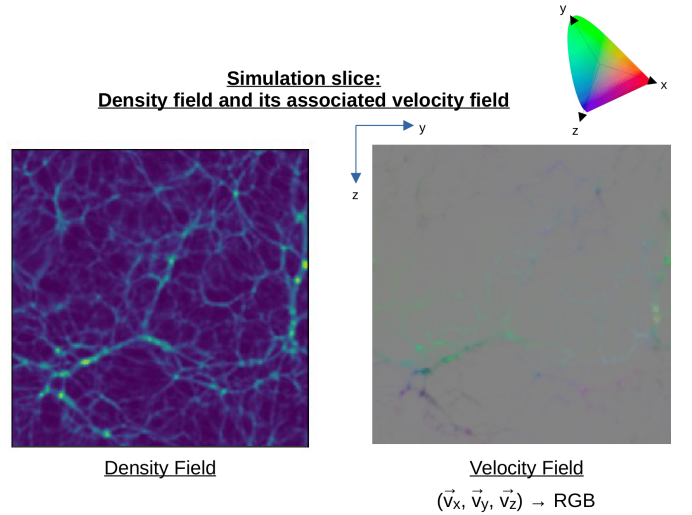


Fig. 8: Example slice of a 3D simulation, showing the density field (*left*) and its associated velocity field (*right*), represented in (v_x, v_y, v_z) to (R,G,B)

Using these data, we train a TW to recover the density field at $z = 0$ from input density + velocity fields (ρ, v_x, v_y, v_z) at redshifts varying from $z = 0$ to $z = 3$ by steps of $\delta z = 1$.

Observing the predicted data (Fig. 10) we note that models yield nearly identical results regardless of the input z . Unsurprisingly, they seem to have the same limitations as the data inferred by the baseline TW with input $z = 0$ (see Fig.6), recovering thicker dense structure more accurately than finer diffuse structure. Indeed, a TW trained with additional information should not exceed the results of an AE provided with all the needed information as input.

As can be expected given the similarity between input and predicted data, the predicted power spectra (Fig. 11, *left*) are

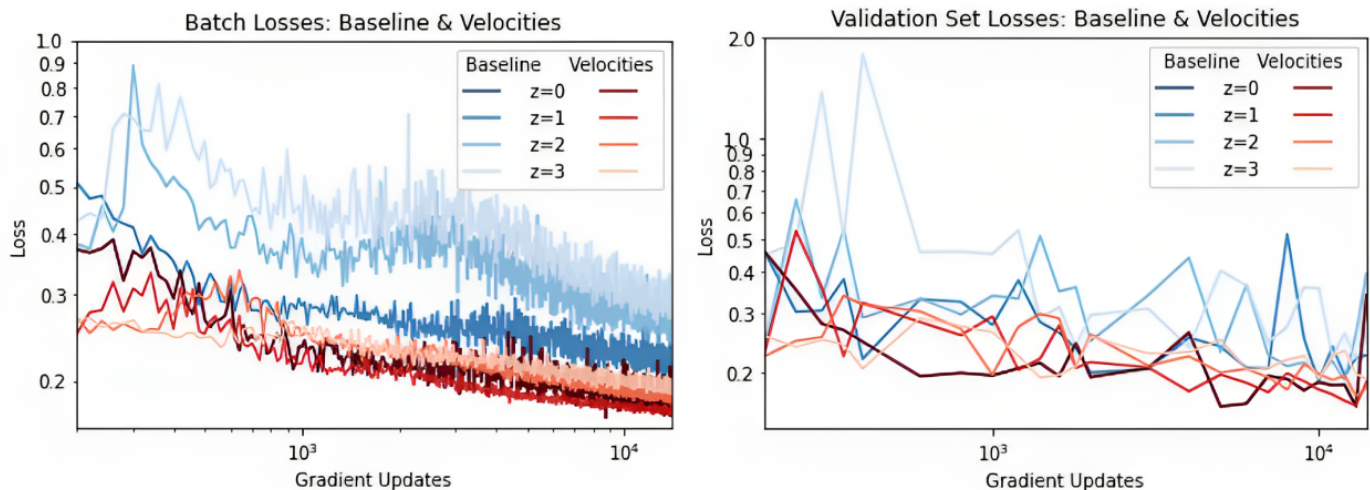


Fig. 9: Batch and validation set losses for the *velocities TW* (red) shown next to those of the *baseline TW* (blue) for training at various input redshifts.

close to the true simulation power spectrum, especially when compared to those recovered by the *baseline TW*.

A study of the dice coefficient (Fig. 11, right) completes the picture by showing that the (density+velocity) TW outperforms the baseline TW, to the point that the recovered dice of the (density+velocity) TW for input $z = 3$ is better than that of the baseline TW with input $z = 1$.

Finally, inspecting the evolution of the loss measured throughout training for both cases (baseline TW and velocities TW, i.e. density only vs density+velocity input, see Fig.9), we can notice a few things. First, past a certain point in training all training losses follow a clear linear trend in log-log. While significantly more noisy, this appears to be the case for validation losses as well. Comparing the two cases, we can note that density-only input training leads to overall greater and noisier loss, suggesting that adding velocity fields to the input makes the task less difficult and the training more stable.

We can conclude that our network’s additional use of initial velocity fields yields significantly improved results. This can be expected as we are providing the necessary ingredients used in established methods like the Zel’dovich approximation for the prediction of cosmic structure formation (Hidding et al. 2014). Indeed the Zel’dovich approximation is linear and relies on initial conditions (here, density and velocity field) and gravitational potential (which can be derived from the density field) to extrapolate the density field well into the non-linear regime. Drawing from this principle, we can expect our model to employ a similar strategy, harnessing the velocity field to refine predictions efficiently.

4. Discussion

4.1. Results

When examining our results, it is interesting to keep in mind the dual task of our TW; indeed, it both needs to encode data with minimal loss of information, and to predict its evolution. Thinking in terms of these two aspects, we can more easily see which task a given TW struggles with most,

in other words its limiting factor. This can in turn guide us into finding efficient methods to ease the TW’s task for optimal results.

Looking at the baseline TW’s results for 2D we find that the prediction aspect works surprisingly well. Similar results on all measures for all input z suggest that the main limiting factor seems to be in the encoding aspect - and thus that future work should focus on developing a better replicative ($z = 0$ to $z = 0$) autoencoder. Existing work (Villaescusa-Navarro et al. 2021) using very efficient AEs for this type of data should be looked into, but the high dimension of the latent space might make it less semantically meaningful, and therefore impact the prediction aspect. Conversely, in 3D, we can clearly observe that predictions become significantly more difficult with growing input z , suggesting this time that the prediction aspect is the primary limiting factor. Indeed, the target encoded data, associated with target output at $z = 0$, should be the same regardless of input z , thus encoding limitations are not expected to change with input.

To make predictions easier, we provide the TW with the input density fields’ associated velocity fields, and find that results are thus significantly improved with - as in the baseline 2D case - comparable prediction results regardless of input z ; the limiting factor seems to become encoding once more.

4.2. Interpretation

We can reformulate our problem to better interpret the results we obtained for these three configurations.

In our case, our TW can be considered as a multi-parameter complex function that is built to transform a density field into another, an injective function from the space of N-body simulations (in a given format) to that of a GAN’s generative space (the subset of data space within which it is constrained to generate). When trying to model such a function, one has to consider both whether this setup is a good description of the physical problem (i.e. is the problem truly injective within the two considered spaces?),

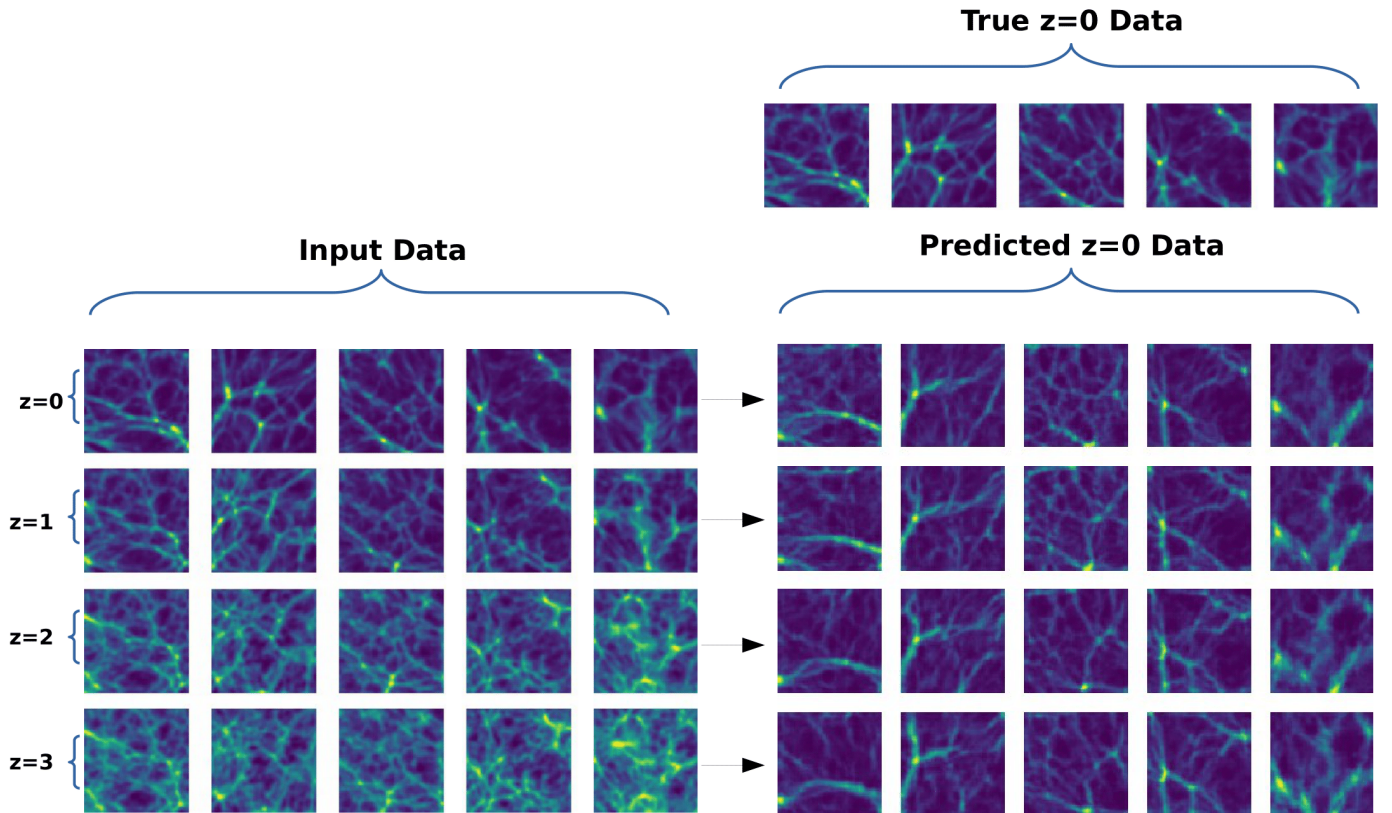


Fig. 10: Five images from the 2D simulations at various redshifts (*left*), and their equivalent predictions of redshift $z = 0$ (*right*) as inferred by the (density+velocity) TW. The true $z = 0$ simulation images are shown above the predicted images (*upper right*) for comparison.

and whether the architecture and training of the TW is fit to model the hypothetical function.

Here, assuming that the hypothetical function is injective equates to assuming the following:

- Every input has a single theoretical ground truth as associated output (one density field at a given z yields a single density field at $z=0$).
- This ground truth can be found within a constrained space (our GAN’s generative space).

On the existence of a single ground truth for a given input
Concerning the first point, one might remark that the same density field can lead to a multiplicity of density fields at a further period, depending on initial conditions that it does not contain, namely initial velocities and neighboring dense structures; thus the best we can expect from our TW is to yield an averaged field that integrates over the unknowns.

This limitation affects the prediction aspect mentioned previously. Moreover, we can expect the discrepancy between this average and the ground truth to grow the further in time we try to predict. If we posit that this is what we can observe in the 3D baseline TW’s increasingly poor predictions with growing input z , providing the velocity fields as additional input should constrain a density field’s evolution much more, not only in terms of providing initial velocities and matter dynamics but also indicating nearby potential

wells attracting mass, leading to more precise predictions (provided that the TW can efficiently use this additional information for inference). Doing this, we find that results are greatly improved, which suggests that our hypothesis is correct.

On existence of the ground truth in generative space
Concerning the second point, it is possible and even likely that the GAN’s generative space does not sufficiently cover the whole range of possible $z = 0$ simulated data; and thus when trying to emulate a ground truth, the TW is limited to outputting the closest existing datum in the GAN’s limited generative space. This limitation can be assimilated to the encoding limitation mentioned previously. Solutions to this include either building a better GAN with a more "all-including" generative space, or removing constraints entirely by not making use of a pretrained GAN to build our TW. This second option is viable and worth looking into, but implies a loss of the output data’s statistical similarity to original simulation data (i.e. better Dice coefficient, but worse power spectrum, pixel pdf, peak counts etc.)

4.3. Further Work

Given these encouraging initial results and our understanding of what might be causing their limitations, further work would include investigating the use of more powerful GANs (notably with a higher-dimension latent space), using an unconstrained decoder and testing existing complex AE

structures. Interesting alternatives could include Variational Autoencoders (VAEs) (Kingma & Welling 2013), which are known to favor semantically meaningful latent spaces, or U-nets (Siddique et al. 2021), which pass on information from encoder to decoder at different scales, implying less loss of information from input to output. We could also look into new ways to simplify the prediction task, by providing a map of the gravitational potential as input, or making use of our knowledge of the problem’s symmetries to choose a better model architecture; indeed we know that our datasets are self-similar and isotropic, and while traditional CNNs are invariant in terms of translation, they are not so in terms of rotation or scale, which implies pointless redundancy in kernel weights. More fine-tuned architectures, of the kind of Bispectral Neural Networks (Sanborn et al. 2022) might be better suited for the task.

Alternatively, we could retain our current AE training structure but apply it to tasks where recovering correct statistics is more crucial, such as denoising or reconstructing masked areas.

Additionally, we have explored other paths to optimize TW results, such as curriculum training (Bengio et al. 2009) or using a set of snapshots at different redshifts as input (e.g. predicting $z = 0$ from two snapshots at $z = 2$ and 3). Though these methods showed improvement on the baseline approach, they were significantly less impressive than those obtained by using the velocity fields and were not included in this article.

Finally, future work should also focus on evolving the density field backward in time, starting by predicting $z = 3$ from various $z < 3$. However, it is crucial to acknowledge that this endeavor is expected to pose greater difficulty compared to forward prediction, given the challenges inherent in solving an inverse problem, notably the non-uniqueness of potential solutions.

5. Conclusion

In this article, we aimed to investigate the ability for a neural network to infer the evolution over time of large-scale density fields.

Using an AE architecture from a previous work, we trained a TW to predict the evolution of simulation-issued density fields from redshifts $z = 1, 2$, and 3 to $z = 0$ for 2D and 3D simulations. We found that for 2D simulation data, the prediction was satisfactory, with similar performance in terms of recovering the power spectrum and true/predicted structure overlap regardless of input z . Conversely, training on 3D density fields showed that predictions were increasingly imprecise with growing input z , both in overall statistics (increasingly dissimilar power spectrum) and individual prediction (decreasing dice coefficient).

We posited that this outcome might arise from the insufficient information provided by the input data to adequately constrain the target data.

Thus in a second step we additionally supplied the TW with the 3D density fields’ associated velocity fields as input to provide more information on matter dynamics, and found that the predictions were greatly improved, with similar results for all input z as in the 2D case.

This significant improvement in performance highlights the TW’s ability to make efficient use of new relevant information, providing minimal guidance in terms of method. This finding underscores the importance of incorporating underlying physics when constructing a model - in this case providing initial matter velocity as well as position to better constrain matter evolution.

Finally, these results are especially promising when considering the relative simplicity of our model. Indeed, while the existing TW’s predictions are noteworthy, we can expect them to be largely improved upon. We outline several possible paths, in the form of alternative architectures and training methods, as well as alternate uses of the model.

In light of the progressive and experimental nature of optimizing such models, it is essential to emphasize the importance of exploring ML models to uncover their possibilities and limitations, irrespective of immediate practicality.

Acknowledgements. The authors thank H. Tanimura for providing the 3D simulations, and the whole ByoPiC (<https://byopic.eu/>) team for fruitful discussions and advice. This project was funded by the European Research Council (ERC) under the European Union’s Horizon 2020 research and innovation programme grant agreement ERC-2015-AdG 695561. M.U. was supported by the Irfu of CEA Saclay, through the PTC program. A.D. was supported by the Comunidad de Madrid and the Complutense University of Madrid (Spain) through the Atracción de Talento program (Ref. 2019-T1/TIC-13298)

References

- Agarwal, S., Davé, R., & Bassett, B. A. 2018, *Monthly Notices of the Royal Astronomical Society*, 478, 3410
- Aragon-Calvo, M. A. 2019, *Monthly Notices of the Royal Astronomical Society*, 484, 5771
- Bengio, Y., Louradour, J., Collobert, R., & Weston, J. 2009, in *Proceedings of the 26th annual international conference on machine learning*, 41–48
- Biswas, M. & Adlak, R. 2018, in *2018 4th International Conference for Convergence in Technology (I2CT)*, IEEE, 1–4
- Bonjean, V. 2020, *Astronomy & Astrophysics*, 634, A81
- Bonjean, V., Aghanim, N., Salomé, P., et al. 2019, *Astronomy & Astrophysics*, 622, A137
- Boylan-Kolchin, M., Springel, V., White, S. D., Jenkins, A., & Lemson, G. 2009, *Monthly Notices of the Royal Astronomical Society*, 398, 1150
- Burke, C. J., Aleo, P. D., Chen, Y.-C., et al. 2019, *Monthly Notices of the Royal Astronomical Society*, 490, 3952
- Chittenden, H. G. & Tojeiro, R. 2023, *Monthly Notices of the Royal Astronomical Society*, 518, 5670
- Conceição, M., Krone-Martins, A., da Silva, A., & Moliné, Á. 2024, *Astronomy & Astrophysics*, 681, A123
- Crain, R. A., Schaye, J., Bower, R. G., et al. 2015, *Monthly Notices of the Royal Astronomical Society*, 450, 1937
- Dere, S., Fatima, M., Jagtap, R., Inamdar, U., & Shardoor, N. B. 2021, in *2021 7th International Conference on Advanced Computing and Communication Systems (ICACCS)*, Vol. 1, IEEE, 702–706
- D’Isanto, A. & Polsterer, K. L. 2018, *Astronomy & Astrophysics*, 609, A111
- Feng, L. 2023, *IEEE Journal on Multiscale and Multiphysics Computational Techniques*, 8, 97
- Freed, M. & Lee, J. 2013, in *2013 International Conference on Computational and Information Sciences*, IEEE, 322–325
- Gardner, J. P., Mather, J. C., Clampin, M., et al. 2006, *Space Science Reviews*, 123, 485
- González, R. E., Muñoz, R. P., & Hernández, C. A. 2018, *Astronomy and computing*, 25, 103
- Hansen, D., Mendoza, I., Liu, R., et al. 2022, *arXiv preprint arXiv:2207.05642*
- Hausen, R. & Robertson, B. 2022, *arXiv preprint arXiv:2201.04714*
- He, S., Li, Y., Feng, Y., et al. 2019, *Proceedings of the National Academy of Sciences*, 116, 13825

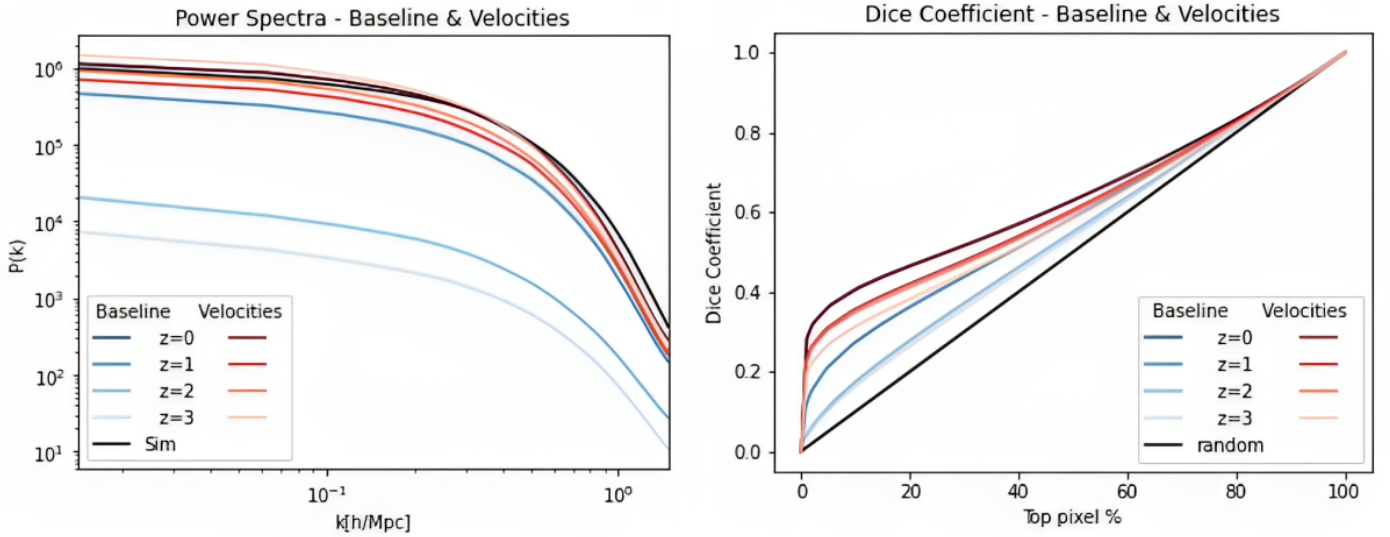


Fig. 11: *Left*: Median power spectra of the data predicted by both by the *velocities TW* (red) and the *baseline TW* (blue) from various input redshifts. The median power spectrum of the true $z = 0$ simulation data is shown in *black*. *Right*: Average dice coefficient between target $z = 0$ 3D simulation data and data as predicted both by the (density+velocity) TW (red) and the *baseline TW* (blue) from various input redshifts.

- Henghes, B., Pettitt, C., Thiyaalingam, J., Hey, T., & Lahav, O. 2021, Monthly Notices of the Royal Astronomical Society, 505, 4847
- Henghes, B., Thiyaalingam, J., Pettitt, C., Hey, T., & Lahav, O. 2022, Monthly Notices of the Royal Astronomical Society, 512, 1696
- Hidding, J., Shandarin, S. F., & van de Weygaert, R. 2014, Monthly Notices of the Royal Astronomical Society, 437, 3442
- Humbird, K. D., Peterson, J. L., & McClarren, R. G. 2018, arXiv preprint arXiv:1811.05852
- Jia, P., Zheng, Y., Wang, M., & Yang, Z. 2023, Astronomy and Computing, 42, 100687
- Jo, Y. & Kim, J.-h. 2019, Monthly Notices of the Royal Astronomical Society, 489, 3565
- Johnson, J., Alahi, A., & Fei-Fei, L. 2016, in Computer Vision—ECCV 2016: 14th European Conference, Amsterdam, The Netherlands, October 11–14, 2016, Proceedings, Part II 14, Springer, 694–711
- Kingma, D. P. & Welling, M. 2013, arXiv preprint arXiv:1312.6114
- Kitaura, F.-S. & Heß, S. 2013, Monthly Notices of the Royal Astronomical Society: Letters, 435, L78
- Kodi Ramanah, D., Charnock, T., Villaescusa-Navarro, F., & Wandelt, B. D. 2020, Monthly Notices of the Royal Astronomical Society, 495, 4227
- Laureijs, R., Amiaux, J., Arduini, S., et al. 2011, arXiv preprint arXiv:1110.3193
- Liu, Y. 2023, International Journal of Modern Physics C, 2350099
- Monaco, P., Theuns, T., & Taffoni, G. 2002, Monthly Notices of the Royal Astronomical Society, 331, 587
- Nelson, D., Springel, V., Pillepich, A., et al. 2019, Computational Astrophysics and Cosmology, 6, 1
- Rastegarnia, F., Mirtorabi, M., Moradi, R., Vafaei Sadr, A., & Wang, Y. 2022, Monthly Notices of the Royal Astronomical Society, 511, 4490
- Reyes, E. & Estévez, P. A. 2020, in 2020 International Joint Conference on Neural Networks (IJCNN), IEEE, 1–8
- Rezaei, S., McKean, J., Biehl, M., de Roo, W., & Lafontaine, A. 2022a, Monthly Notices of the Royal Astronomical Society, 517, 1156
- Rezaei, S., McKean, J. P., Biehl, M., & Javadpour, A. 2022b, Monthly Notices of the Royal Astronomical Society, 510, 5891
- Sanborn, S., Shewmake, C., Olshausen, B., & Hillar, C. 2022, arXiv preprint arXiv:2209.03416
- Sanchez-Gonzalez, A., Godwin, J., Pfaff, T., et al. 2020, in International conference on machine learning, PMLR, 8459–8468
- Shamir, L. 2009, Monthly Notices of the Royal Astronomical Society, 399, 1367
- Shandarin, S. F. & Zeldovich, Y. B. 1989, Reviews of Modern Physics, 61, 185
- Siddique, N., Paheding, S., Elkin, C. P., & Devabhaktuni, V. 2021, Ieee Access, 9, 82031
- Springel, V. 2005, Monthly notices of the royal astronomical society, 364, 1105
- Springel, V., Yoshida, N., & White, S. D. 2001, New Astronomy, 6, 79
- Sweere, S. F., Valtchanov, I., Lieu, M., et al. 2022, Monthly Notices of the Royal Astronomical Society, 517, 4054
- Tanimura, H., Aghanim, N., Bonjean, V., & Zaroubi, S. 2022, Astronomy & Astrophysics, 662, A48
- Tassev, S., Zaldarriaga, M., & Eisenstein, D. J. 2013, Journal of Cosmology and Astroparticle Physics, 2013, 036
- Ullmo, M., Decelle, A., & Aghanim, N. 2021, Astronomy & Astrophysics, 651, A46
- Vafaei Sadr, A., Vos, E. E., Bassett, B. A., et al. 2019, Monthly Notices of the Royal Astronomical Society, 484, 2793
- Villaescusa-Navarro, F., Anglés-Alcázar, D., Genel, S., et al. 2021, The Astrophysical Journal, 915, 71
- Villar, V. A., Cranmer, M., Berger, E., et al. 2021, The Astrophysical Journal Supplement Series, 255, 24
- Vogelsberger, M., Genel, S., Springel, V., et al. 2014, Monthly Notices of the Royal Astronomical Society, 444, 1518
- Wiewel, S., Becher, M., & Thuerey, N. 2019, in Computer graphics forum, Vol. 38, Wiley Online Library, 71–82
- Wilde, J., Serjeant, S., Bromley, J. M., et al. 2022, Monthly Notices of the Royal Astronomical Society, 512, 3464
- Wu, J. F. & Jespersen, C. K. 2023, arXiv preprint arXiv:2306.12327